Supporting Information

Optoelectronic and Energy Level Exploration of Bismuth and Antimony-Based Materials for Lead-Free Solar Cells

Ryosuke Nishikubo[†], *Hiroyuki Kanda*[‡], *Inés García-Benito*[‡, §], *Agustín Molina-Ontoria*[//], *Gianluca Pozzi*[⊥], *Abdullah M. Asiri*[#], *Mohammad Khaja Nazeeruddin*[*, ‡], *and Akinori Saeki*[*, †, ▽]

[†] Department of Applied Chemistry, Graduate School of Engineering, Osaka University, 2-1 Yamadaoka, Suita, Osaka 565-0871, Japan.
[‡] Institute of Chemical Sciences and Engineering, École Polytechnique Fédérale de Lausanne Valais Wallis, Rue de l'Industrie 17, 1950 Sion, Switzerland.
[§] Departamento de Química Organica I, Facultad de Ciencias Químicas, Universidad Complutense de Madrid, 28040 Madrid, Spain.
[//] IMDEA-Nanociencia, C/ Faraday, 9 Ciudad Universitaria de Cantoblanco, 28049 Madrid, Spain.
[⊥] Institute of Chemical Sciences and Technologies-National Research Council (SCITEC-CNR), 20133 Milano, Italy.
[#] Center of Excellence for Advanced Materials Research (CEAMR), King Abdulaziz University, P.O. Box 80203, 21589 Jeddah, Saudi Arabia.
[▽] Precursory Research for Embryonic Science and Technology (PRESTO), Japan Science and Technology Agency, 4-1-8 Honcho, Kawaguchi, Saitama 332-0012, Japan.

AUTHOR INFORMATION
Corresponding Author
*Mohammad Khaja Nazeeruddin; Email: mdkhaja.nazeeruddin@epfl.ch
*Akinori Saeki; Email: saeki@chem.eng.osaka-u.ac.jp

This supporting information presents the following contents.
Supporting Table S1–S5
Supporting Figures S1–S19
Supporting References S1–S8

Supporting Tables

Table S1. Categorized class of crystal structures evaluated from XRD measurements. (A) without contamination, (B) including a little contamination, (C) including dominant contamination, and (U) crystal structures are unable to be resolved due to the lack of reference or amorphous nature.

Crystal structure	Precursor	Class	reference[a]	Precursor	Class	reference[a]
$A_3M_2X_9$	$Cs_3Bi_2I_9$	A	COD: 8103859	$Cs_3Sb_2I_9$	A	COD: 1537132
	$MA_3Bi_2I_9$	A	COD: 4344961	$MA_3Sb_2I_9$	A	COD: 7237225
	$FA_3Bi_2I_9$	A	COD: 7237621	$FA_3Sb_2I_9$	A	Ref. S2
	$Cs_3Bi_2Br_9$	A	COD: 1531067	$Cs_3Sb_2Br_9$	A	COD: 1537138
	$MA_3Bi_2Br_9$	A	Ref. S1	$MA_3Sb_2Br_9$	A	Ref. S3
	$FA_3Bi_2Br_9$	A	COD: 7701111	$FA_3Sb_2Br_9$	A	-
MSX	BiSI	B	COD: 1535800	SbSI	A	COD: 1535787
	BiSBr	A	COD: 1535795	SbSBr	U	COD: 1521208
Layered	Bi_2S_3	A	COD: 9003473	Sb_2S_3	A	COD: 1011154
	$AgBiI_4$	A	Ref. S4	$AgSbI_4$	U	-
DP	Cs_2AgBiI_6	C	-	Cs_2AgSbI_6	C	-
	MA_2AgBiI_6	C	-	MA_2AgSbI_6	C	-
	FA_2AgBiI_6	C	-	FA_2AgSbI_6	C	-
	$Cs_2AgBiBr_6$	A	COD: 4131244	$Cs_2AgSbBr_6$	B	Ref. S6
	$MA_2AgBiBr_6$	A	Ref. S5	$MA_2AgSbBr_6$	C	
	$FA_2AgBiBr_6$	U	-	$FA_2AgSbBr_6$	C	-
SAP	$CsBiSI_2$	C	-	$CsSbSI_2$	U	-
	$MABiSI_2$	C	-	$MASbSI_2$	B	Ref. S7
	$FABiSI_2$	C	-	$FASbSI_2$	C	-
	$CsBiSBr_2$	C	-	$CsSbSBr_2$	C	-
	$MABiSBr_2$	C	-	$MASbSBr_2$	C	-
	$FABiSBr_2$	C	-	$FASbSBr_2$	C	-

[a] Crystallography Open Database (COD) number or the reference number in the main text.

Table S2. Summary of elemental analysis by EDX on the compositions which showed dominant formation of other crystal phase such as $A_3M_2X_9$ in Figure S1. Note that MA and FA which is composed of C, N, and H cannot be detected.

Precursor	Elemental ratio	Precusor	Elemental ratio
SbSI (240 ℃)	Sb : S : I = 1.0 : 0.89 : 0.89	$CsBiSI_2$	Cs : Bi : S : I = 0.92 : 1.0 : 0.72 : 2.4
SbSBr(240℃)	Sb : S : Br = 1.0 : 0.42 : 1.5	$MABiSI_2$	Bi : S : I = 1.0 : 0.46 : 2.2
Cs_2AgBiI_6	Cs : Ag : Bi : I = 1.6 : 0.97 : 1.0 : 4.8	$FABiSI_2$	Bi : S : I = 1.0 : 0.35 : 2.2
MA_2AgBiI_6	Ag : Bi : I = 0.90 : 1.0 : 5.1	$CsBiSBr_2$	Cs : Bi : S : Br = 0.84 : 1.0 : 0.77 : 2.8
FA_2AgBiI_6	Ag : Bi : I = 0.93 : 1.0 : 5.1	$MABiSBr_2$	Bi : S : Br = 1.0 : 0.52 : 2.6
Cs_2AgSbI_6	Cs : Ag : Sb : I]= 2.0 : 0.98 : 1.0 : 5.0	$FABiSBr_2$	Bi : S : Br = 1.0 : 0.54 : 2.5
MA_2AgSbI_6	Ag : Bi : I = 0.94 : 1.0 : 5.3	$MASbSI_2$	Sb : S : I = 1.0 : 1.0 : 1.6
FA_2AgSbI_6	Ag : Bi : I = 0.98 : 1.0 : 5.4	$FASbSI_2$	Sb : S : I = 1.0 : 0.62 : 1.5
$MA_2AgSbBr_6$	Ag : Bi : Br = 0.83 : 1.0 : 6.3	$FASbSBr_2$	Sb : S : Br = 1.0 : 0.77 : 2.7
$FA_2AgSbBr_6$	Ag : Bi : Br = 0.74 : 1.0 : 7.1		

Table S3. Summary of calculated Goldschmidt tolerance factors (T) of DPs and SAPs. The equation is followed; $T = (r_A + r_X)/(2^{1/2}(r_B + r_X))$ where r_A, r_B, and r_X are the effective ionic radii of A site, B site, and X site ion, respectively.

Structure	Bi-based	T	Sb-based	T
DP	Cs_2AgBiI_6	0.876	Cs_2AgSbI_6	0.914
	MA_2AgBiI_6	0.939	MA_2AgSbI_6	0.979
	FA_2AgBiI_6	1.02	FA_2AgSbI_6	1.06
	$Cs_2AgBiBr_6$	0.890	$Cs_2AgSbBr_6$	0.931
	$MA_2AgBiBr_6$	0.958	$MA_2AgSbBr_6$	1.00
	$FA_2AgBiBr_6$	1.04	$FA_2AgSbBr_6$	1.09
SAP	$CsBiSI_2$	0.928	$CsSbSI_2$	1.02
	$MABiSI_2$	0.994	$MASbSI_2$	1.08
	$FABiSI_2$	1.08	$FASbSI_2$	1.18
	$CsBiSBr_2$	0.920	$CsSbSBr_2$	1.01
	$MABiSBr_2$	0.990	$MASbSBr_2$	1.09
	$FABiSBr_2$	1.08	$FASbSBr_2$	1.18

Table S4. Summary of VBM, CBM, and bandgap evaluated by PYS, VBM+bandgap, and Tauc plots of photoabsorption spectra of films (direct transition: $(\alpha h\nu)^2$, indirect transition: $(\alpha h\nu)^{0.5}$), respectively.

Materials	VBM (eV)	CBM (eV)	Bandgap (eV)
$MAPbI_3$	–5.45	–3.83	1.62
TiO_2	–7.40	–4.20	3.20
PTAA	–5.17	–2.16	3.01
$Cs_3Bi_2I_9$	–5.83	–3.78	2.05
$MA_3Bi_2I_9$	–5.93	–3.71	2.16
$FA_3Bi_2I_9$	–6.10	–3.9	2.21
$Cs_3Bi_2Br_9$	–6.30	–3.63	2.67
$MA_3Bi_2Br_9$	–6.28	–3.55	2.73
$FA_3Bi_2Br_9$	–5.78	–3.07	2.71
BiSI	–6.20	–4.6	1.60
BiSBr	–5.90	–3.95	1.95
Bi_2S_3	–5.50	–4.10	1.40
$AgBiI_4$	–6.00	–4.20	1.80
$Cs_3Bi_2I_9$ from Cs_2AgBiI_6 precursor	–5.83	–3.63	2.20
$MA_3Bi_2I_9$ from MA_2AgBiI_6 precursor	–5.71	–3.51	2.20
$FA_3Bi_2I_9$ from FA_2AgBiI_6 precursor	–5.90	–3.67	2.23
$Cs_2AgBiBr_6$	–5.95	–3.41 (–3.65)[a]	2.54 (2.30)[a]
$MA_2AgBiBr_6$	–5.90	–3.21 (–3.29)[a]	2.69 (2.61)[a]
$FA_2AgBiBr_6$	–5.97	–3.04	2.93
$Cs_3Bi_2I_9$ from $CsBiSI_2$ precursor	–5.71	–4.01	1.70
$MA_3Bi_2I_9$ from $MABiSI_2$ precursor	–6.14	–4.38	1.76
$FA_3Bi_2I_9$ from $FABiSI_2$ precursor	–6.1	–4.36	1.74
$Cs_3Bi_2Br_9$ from $CsBiSBr_2$ precursor	–6.01	–4.10	1.91
$MA_3Bi_2Br_9$ from $MABiSBr_2$ precursor	–6.1	–4.31	1.79
$FA_3Bi_2Br_9$ from $FABiSBr_2$ precursor	–5.94	–4.19	1.75
$Cs_3Sb_2I_9$	–5.51	–3.32	2.19
$MA_3Sb_2I_9$	–5.56	–3.36	2.20
$FA_3Sb_2I_9$	–5.76	–3.44	2.32
$Cs_3Sb_2Br_9$	–5.81	–3.22	2.59
$MA_3Sb_2Br_9$	–6.1	–3.47	2.63
$FA_3Sb_2Br_9$	–6.03	–3.30	2.73
SbSI	–5.67	–3.52	2.15
SbSI (240 °C)	–5.84	–4.12	1.72
Sb-S-Br (240 °C)	–5.78	–3.69	2.09
Sb_2S_3	–5.62	–3.97	1.68
$AgSbI_4$	–5.95	–3.75	2.20

$Cs_3Sb_2I_9$ from Cs_2AgSbI_6 precursor	–5.41	–3.14	2.27
$MA_3Sb_2I_9$ from MA_2AgSbI_6 precursor	–5.45	–3.07	2.38
$FA_3Sb_2I_9$ from FA_2AgSbI_6 precursor	–5.92	–3.46	2.46
$Cs_2AgSbBr_6$	–5.64	–3.24 (–3.51)[a]	2.40 (2.13)[a]
$MA_3Sb_2Br_9$ from $MA_2AgSbBr_6$ precursor	–5.66	–2.92	2.74
$FA_3Sb_2Br_9$ from $FA_2AgSbBr_6$ precursor	–5.80	–2.93	2.87
$CsSbSI_2$	–5.54	–3.56	1.98
$MASbSI_2$	–5.55	–3.57	1.98
$FA_3Sb_2I_9$ from $FASbSI_2$ precursor	–5.68	–3.26	2.42
$Cs_3Sb_2Br_9$ from $CsSbSBr_2$ precursor	–5.82	–3.38	2.44
$MA_3Sb_2Br_9$ from $MASbSBr_2$ precursor	–5.87	–3.43	2.44
$FA_3Sb_2Br_9$ from $FASbSBr_2$ precursor	–5.77	–3.83	1.94

[a] The values in brackets are indirect transition-based bandgap and CBM. Most of the films show no significant difference in bandgap analyzed by direct and indirect transition.

Table S5. Summary of solar cell performances.

	HTM: PTAA					HTM: PCPDTBT				
Materials	J_{SC} (mA cm^{-2})	J_{SC} / J_{SC_max} [a]	V_{OC} (V)	FF	PCE (%)	J_{SC} (mA cm^{-2})	J_{SC} / J_{SC_max} [a]	V_{OC} (V)	FF	PCE (%)
$Cs_3Bi_2I_9$	0.082	0.0061	0.29	0.37	8.9×10^{-3}	0.41	0.030	0.48	0.49	0.098
$MA_3Bi_2I_9$	0.12	0.0097	0.34	0.41	0.016	0.55	0.045	0.38	0.48	0.1
BiSI	0.19	0.0085	0.0024	0.085	4.0×10^{-5}	0.078	0.012	0.032	0.27	6.5×10^{-4}
BiSBr	0	0	0	0	0	0.36	0.037	0.003	0.16	2.0×10^{-4}
Bi_2S_3	0	0	0	0	0	0	0	0	0	0
$AgBiI_4$	2.4	0.149	0.49	0.55	0.65	2.9	0.18	0.47	0.59	0.78
$Cs_3Bi_2I_9$ from Cs_2AgBiI_6 precursor	0.073	0.011	0.35	0.42	0.011	0.26	0.056	0.34	0.56	0.05
$MA_3Bi_2I_9$ from MA_2AgBiI_6 precursor	0.24	0.035	0.48	0.5	0.057	0.48	0.070	0.39	0.65	0.12
$FA_3Bi_2I_9$ from FA_2AgBiI_6 precursor	0.028	0.0041	0.13	0.38	1.4×10^{-3}	0.0051	0.0074	0.19	0.35	3.4×10^{-3}
$Cs_2AgBiBr_6$	1.2	0.22	0.95	0.67	0.76	1.1	0.20	0.46	0.59	0.31
$Cs_3Bi_2I_9$ from $CsBiSI_2$ precursor	0.078	0.0074	0.032	0.27	6.5×10^{-4}	0.90	0.086	0.23	0.37	0.077
$MA_3Bi_2I_9$ from $MABiSI_2$ precursor	0.19	0.014	0.036	0.27	1.9×10^{-3}	0.29	0.020	0.012	0.22	7.6×10^{-4}
$FA_3Bi_2I_9$ from $FABiSI_2$ precursor	0.017	0.0019	0.11	0.36	7.1×10^{-4}	0.48	0.053	0.22	0.39	0.041
$Cs_3Bi_2Br_9$ from $CsBiSBr_2$ precursor	0.042	0.014	0.012	0.25	1.2×10^{-4}	0.6	0.19	0.062	0.27	0.01

$MA_3Bi_2Br_9$ from $MABiSBr_2$ precursor	0.032	0.0025	0.0059	0.16	3.1×10^{-5}	0.83	0.065	0.017	0.23	3.2×10^{-3}
$FA_3Bi_2Br_9$ from $FABiSBr_2$ precursor	0.41	0.0018	0.14	0.34	0.019	0.022	0.033	0.1	0.36	8.1×10^{-4}
$Cs_3Sb_2I_9$	0.14	0.020	0.24	0.6	0.021	0.62	0.086	0.37	0.44	0.1
$MA_3Sb_2I_9$	0.18	0.039	0.32	0.49	0.028	0.46	0.099	0.29	0.54	0.074
SbSI (200 °C)	0.31	0.028	0.20	0.37	0.023	3.4	0.31	0.31	0.38	0.40
SbSI (240 °C)	0.67	0.051	0.42	0.56	0.16	7.1	0.57	0.37	0.53	1.35
Sb-S-Br (240 °C)	0.33	0.040	0.41	0.56	0.076	5.2	0.62	0.4	0.53	1.1
Sb_2S_3	6.1	0.35	0.41	0.39	0.98	9	0.51	0.29	0.44	1.16
$AgSbI_4$	0.17	0.092	0.32	0.56	0.031	0.9	0.18	0.33	0.59	0.17
$Cs_3Sb_2I_9$ from Cs_2AgSbI_6 precursor	0.15	0.039	0.34	0.46	0.023	0.62	0.16	0.25	0.56	0.087
$MA_3Sb_2I_9$ from MA_2AgSbI_6 precursor	0.21	0.058	0.39	0.52	0.044	0.31	0.085	0.31	0.59	0.057
$Cs_2AgSbBr_6$	0.29	0.061	0.46	0.5	0.068	0.53	0.11	0.37	0.45	0.088
$CsSbSI_2$	1.5	0.022	0.43	0.47	0.31	4.6	0.025	0.38	0.53	0.92
$MASbSI_2$	0.8	0.11	0.35	0.46	0.13	2.6	0.34	0.22	0.48	0.27
$FA_3Sb_2Br_9$ from $FASbSBr_2$ precursor	0.32	0.079	0.31	0.42	0.04	1.24	0.26	0.24	0.44	0.13

[a] J_{SC_max} is the maximum J_{SC} calculated from the transmittance of $mpTiO_2$/active layer and sunlight spectrum. See Figure S14.

Supporting Figures.

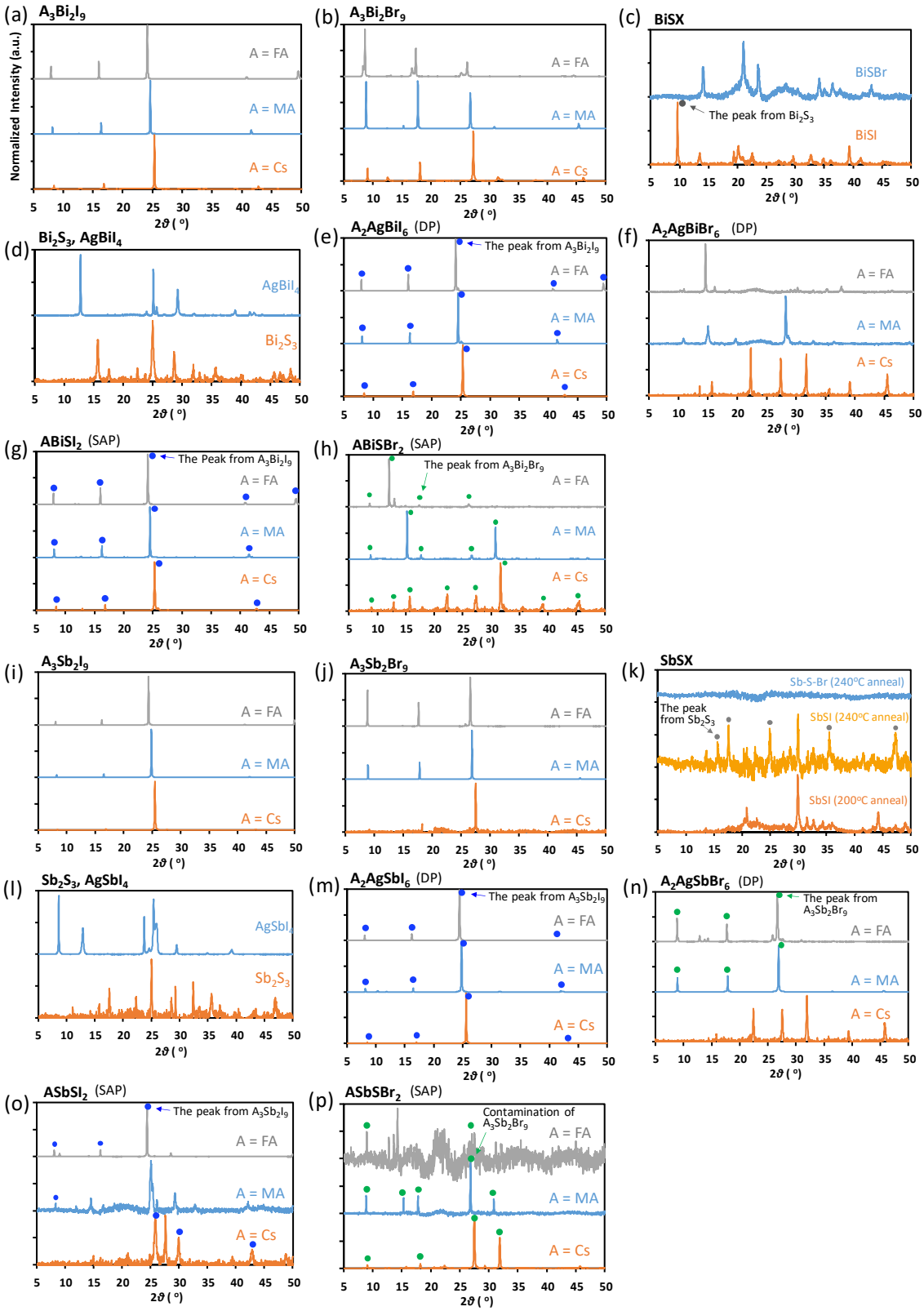

Figure S1. XRD patterns. Contamination of other crystal phases such as $A_3M_2X_9$ is given by the dots.

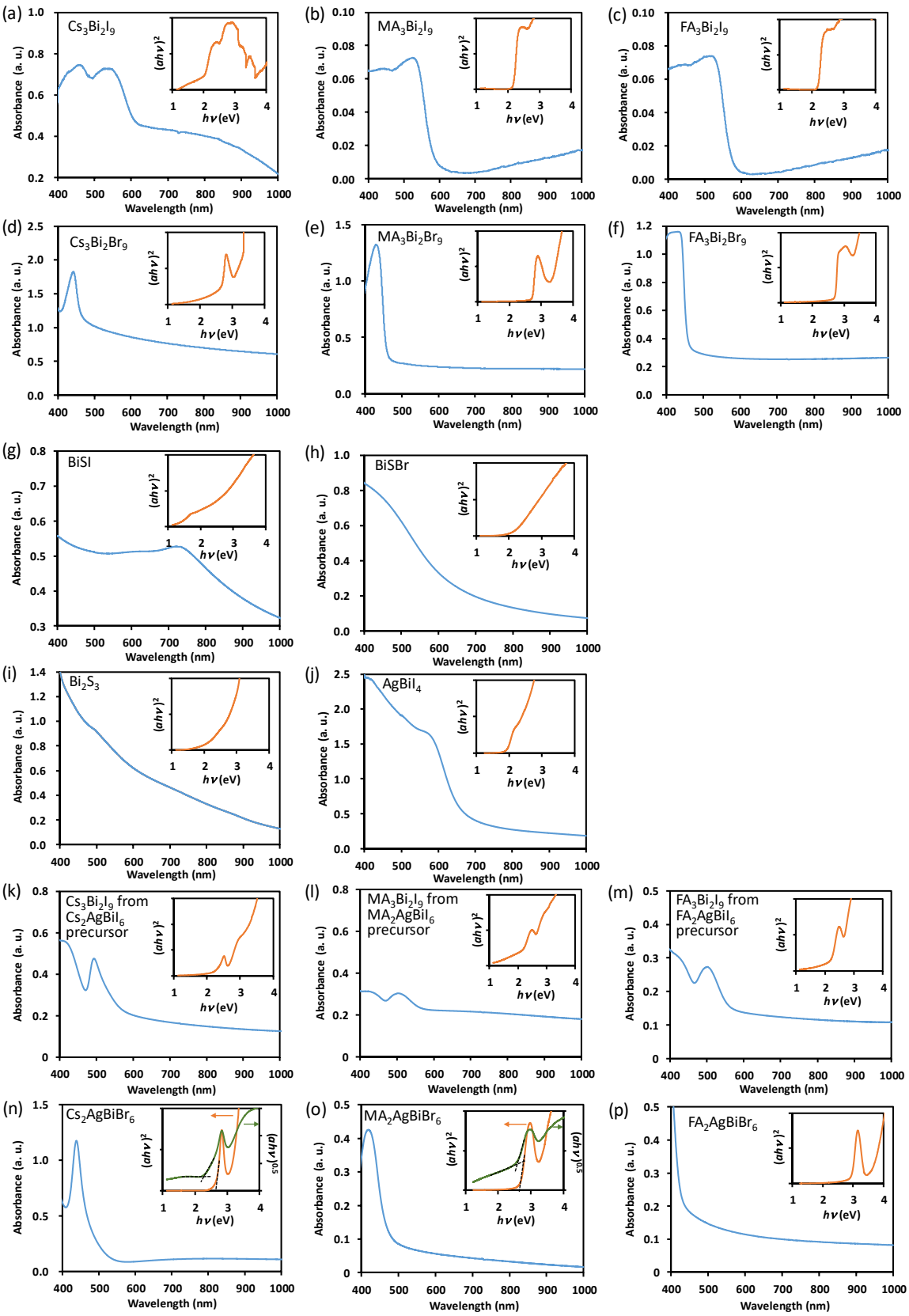

Figure S2. UV-vis photoabsorption spectra (blue line). The samples were prepared on quartz substrates. The insets are the Tauc plots (direct transition: $(\alpha h\nu)^2$ as orange lines, indirect transition: $(\alpha h\nu)^{0.5}$ as green lines).

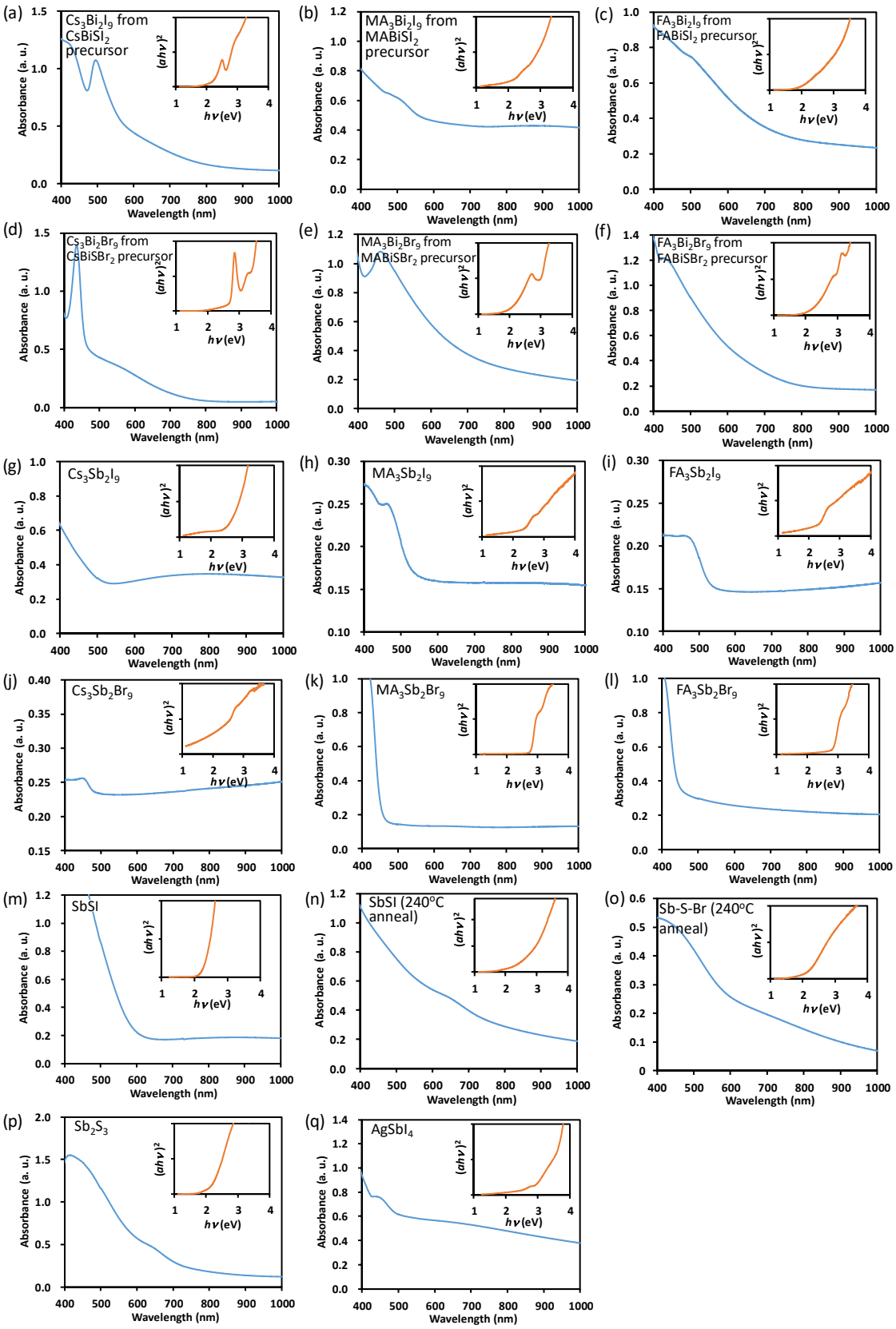

Figure S3. UV-vis photoabsorption spectra (blue line). The samples were prepared on quartz substrates. The insets are the Tauc plots (direct transition: $(\alpha h\nu)^2$ as orange lines, indirect transition: $(\alpha h\nu)^{0.5}$ as green lines).

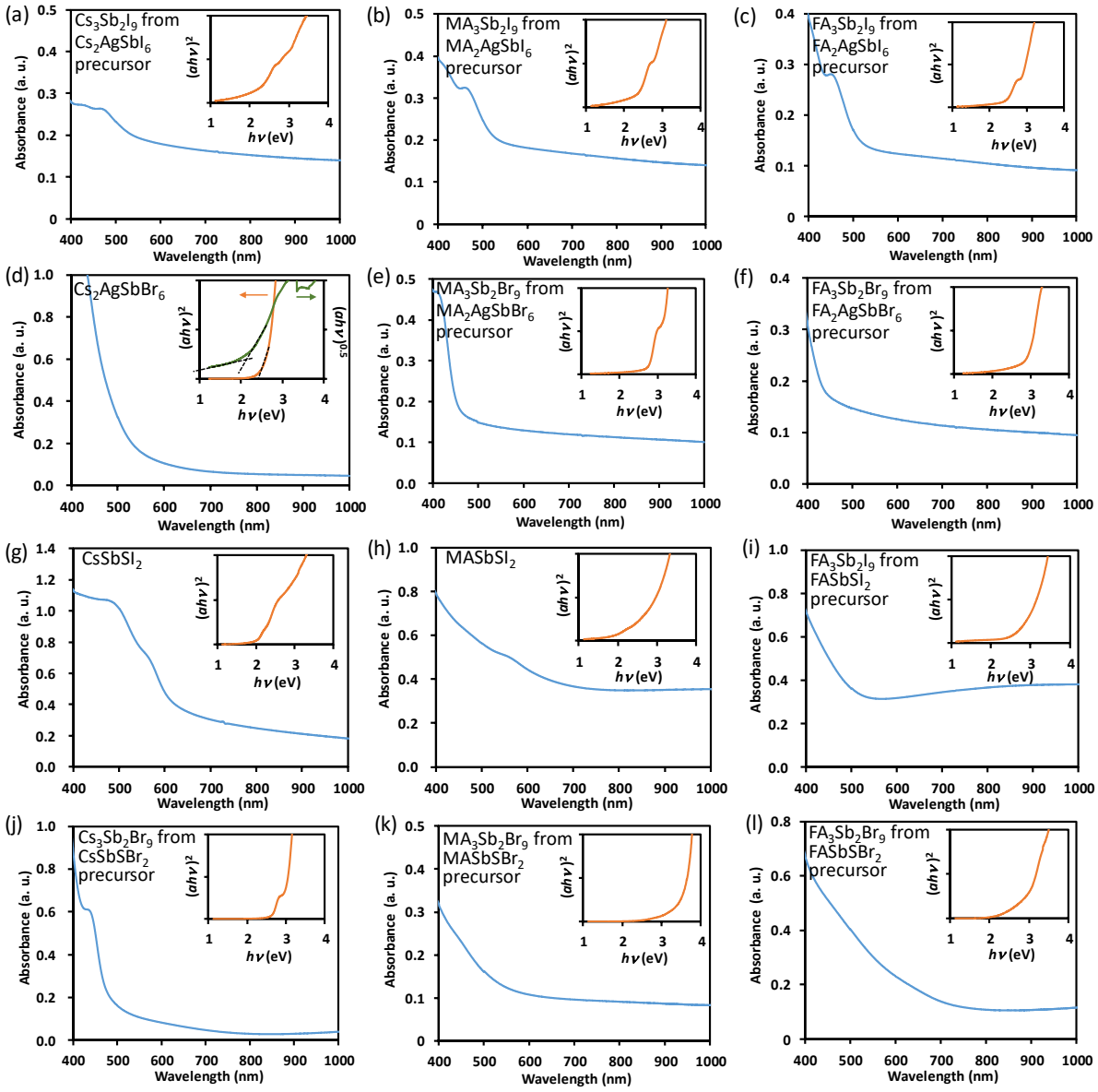

Figure S4. UV-vis photoabsorption spectra (blue line). The samples were prepared on quartz substrates. The insets are the Tauc plots (direct transition: $(\alpha h\nu)^2$ as orange lines, indirect transition: $(\alpha h\nu)^{0.5}$ as green lines).

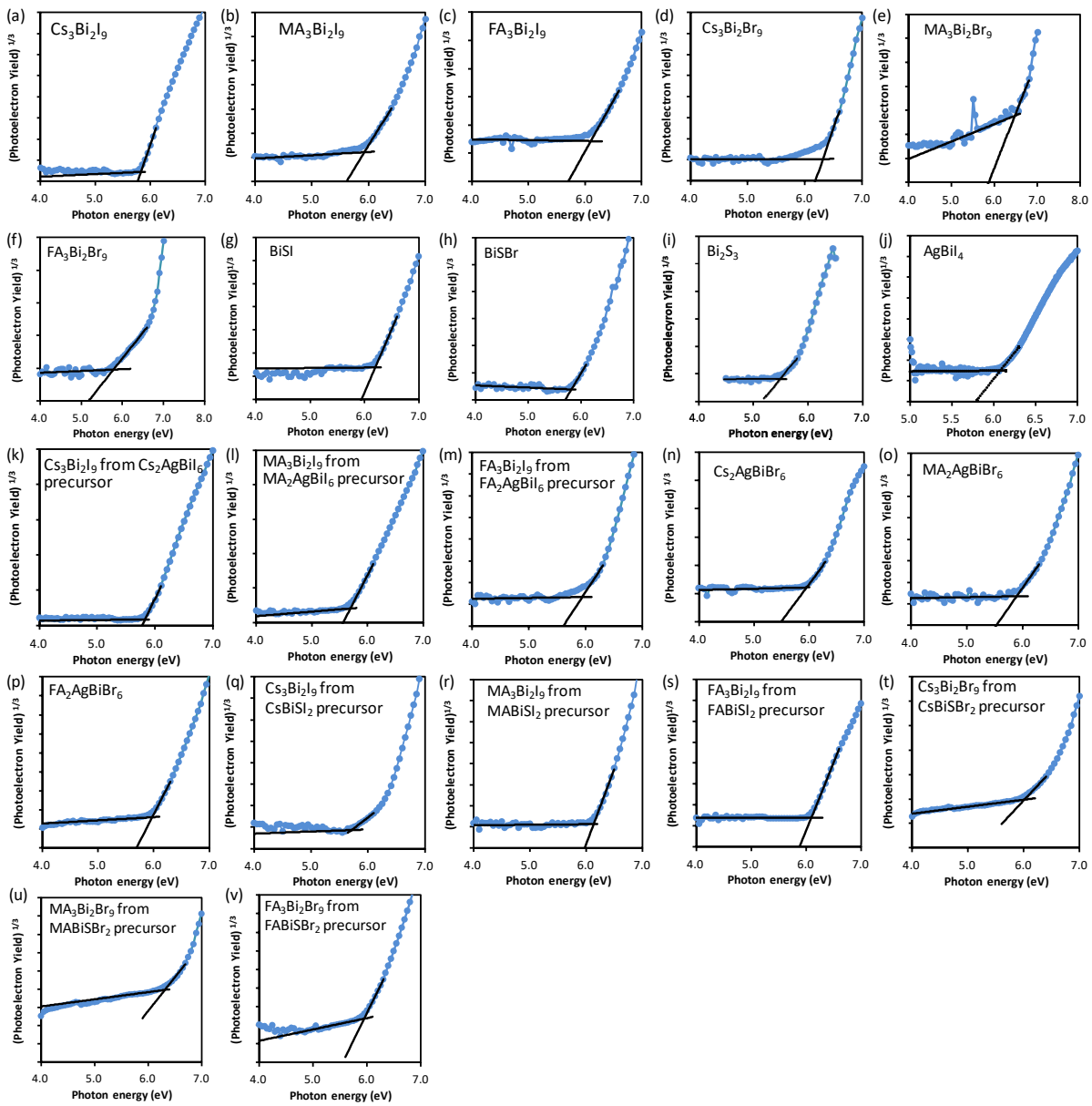

Figure S5. PYS spectra. The samples were prepared on FTO substrates.

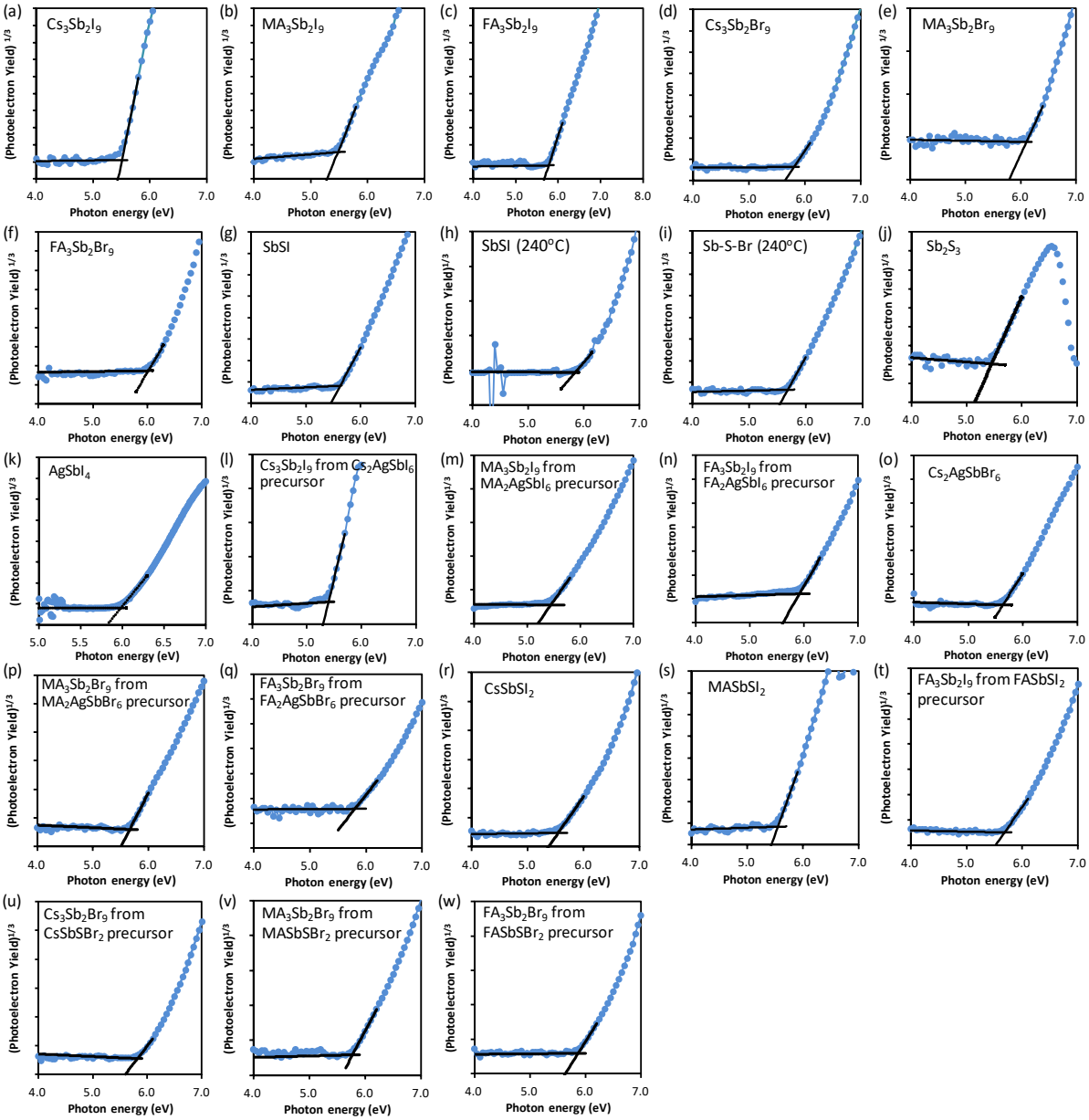

Figure S6. PYS spectra. The samples were prepared on FTO substrates.

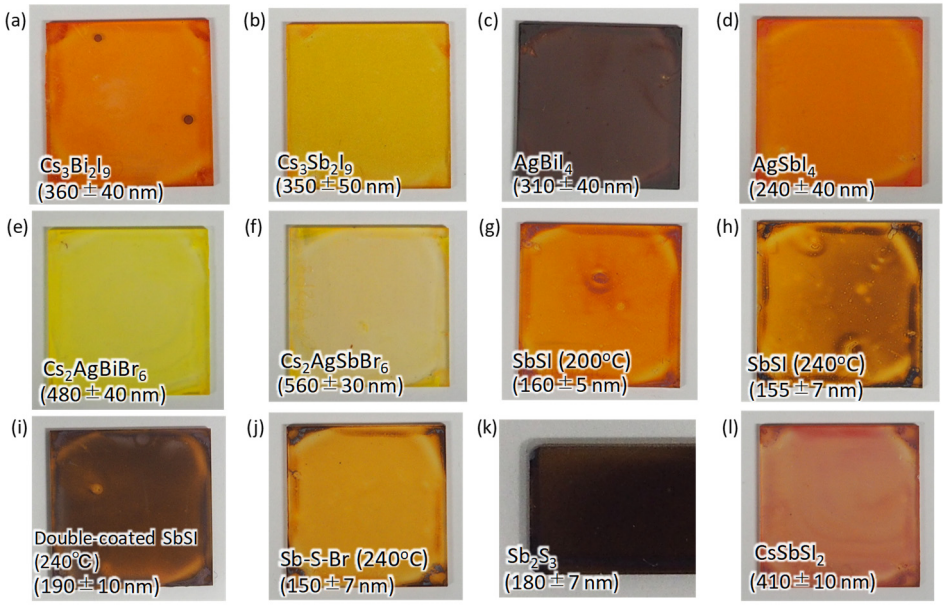

Figure S7. Pictures of $Cs_3Bi_2I_9$, $MA_3Bi_2I_9$, $AgBiI_4$, $AgSbI_4$, $Cs_2AgBiBr_6$, $Cs_2AgSbBr_6$, SbSI (200 °C), Sb_2S_3-containing SbSI (240 °C), double-coated SbSI, Sb-S-Br (240 °C annealed), Sb_2S_3, and $CsSbSI_2$ films. The film thickness of active layer/mp-TiO_2 with a standard deviation is appended in brackets. The thickness of mp-TiO_2 is 145 ± 7 nm.

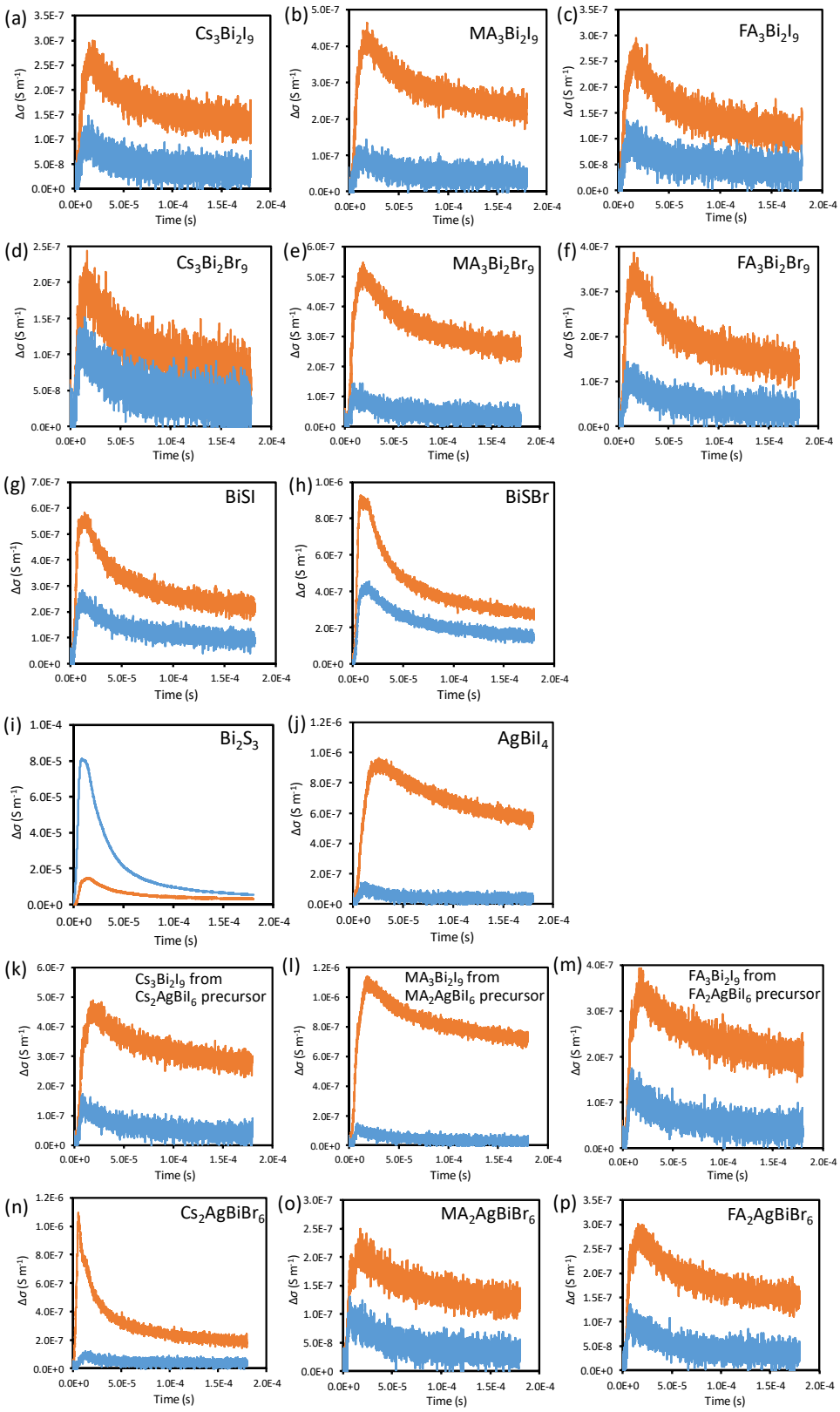

Figure S8. Xe-flash TRMC decays of the films on mp-TiO_2/quartz (orange line) and bare quartz (blue line). All the measurements were conducted in air.

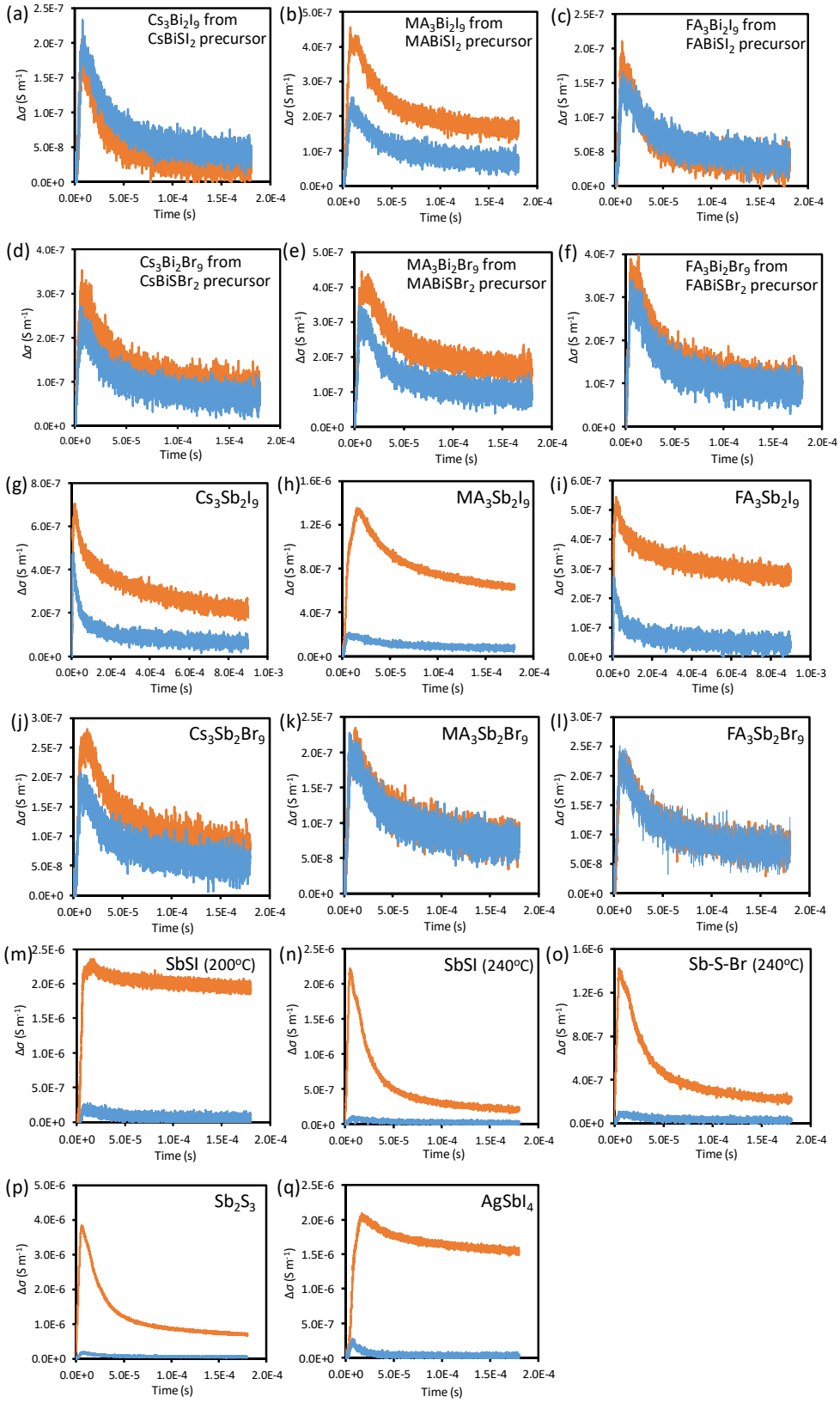

Figure S9. Xe-flash TRMC decays of films on mp-TiO_2/quartz (orange line) and bare quartz (blue line). All the measurements were conducted in air.

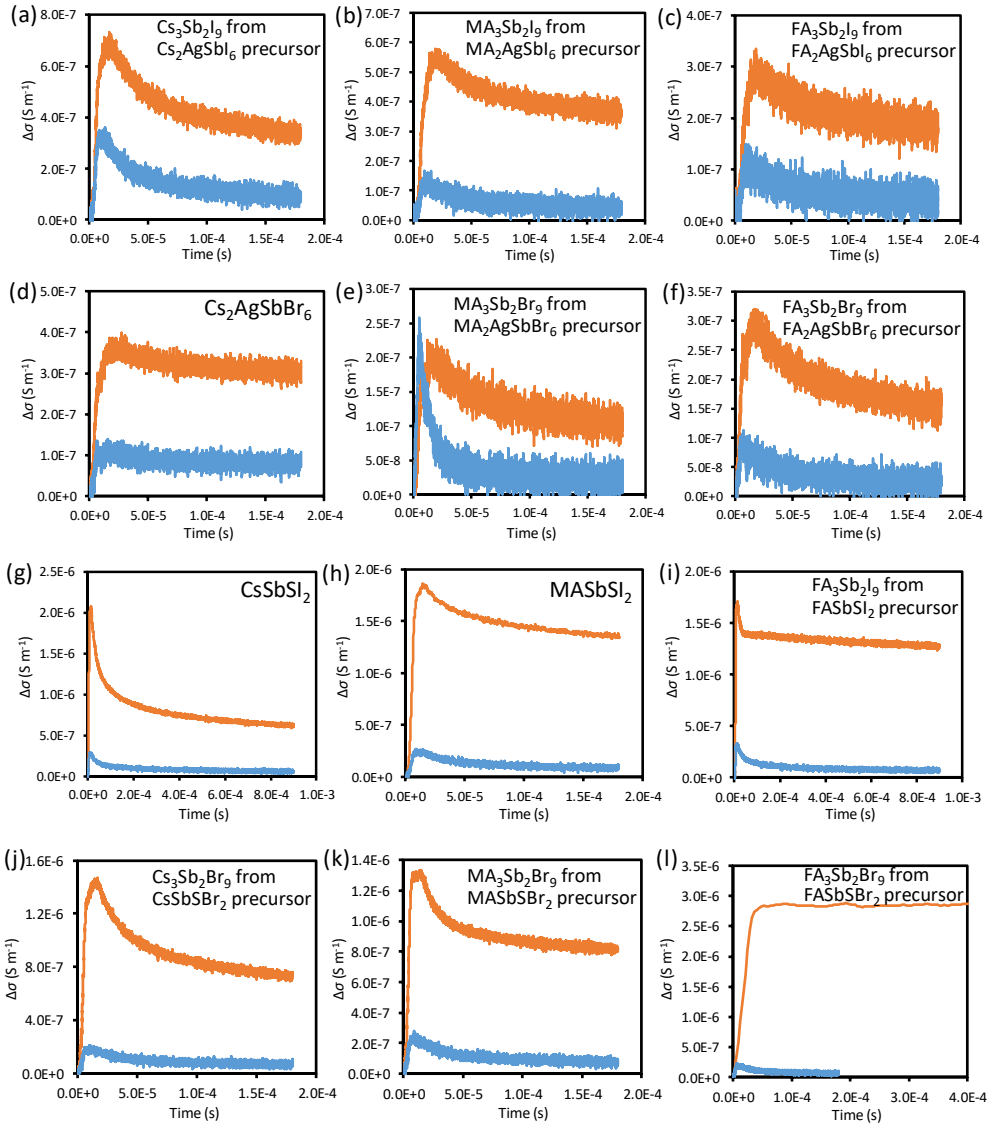

Figure S10. Xe-flash TRMC decays of films on mp-TiO_2/quartz (orange line) and bare quartz (blue line). All the measurements were conducted in air.

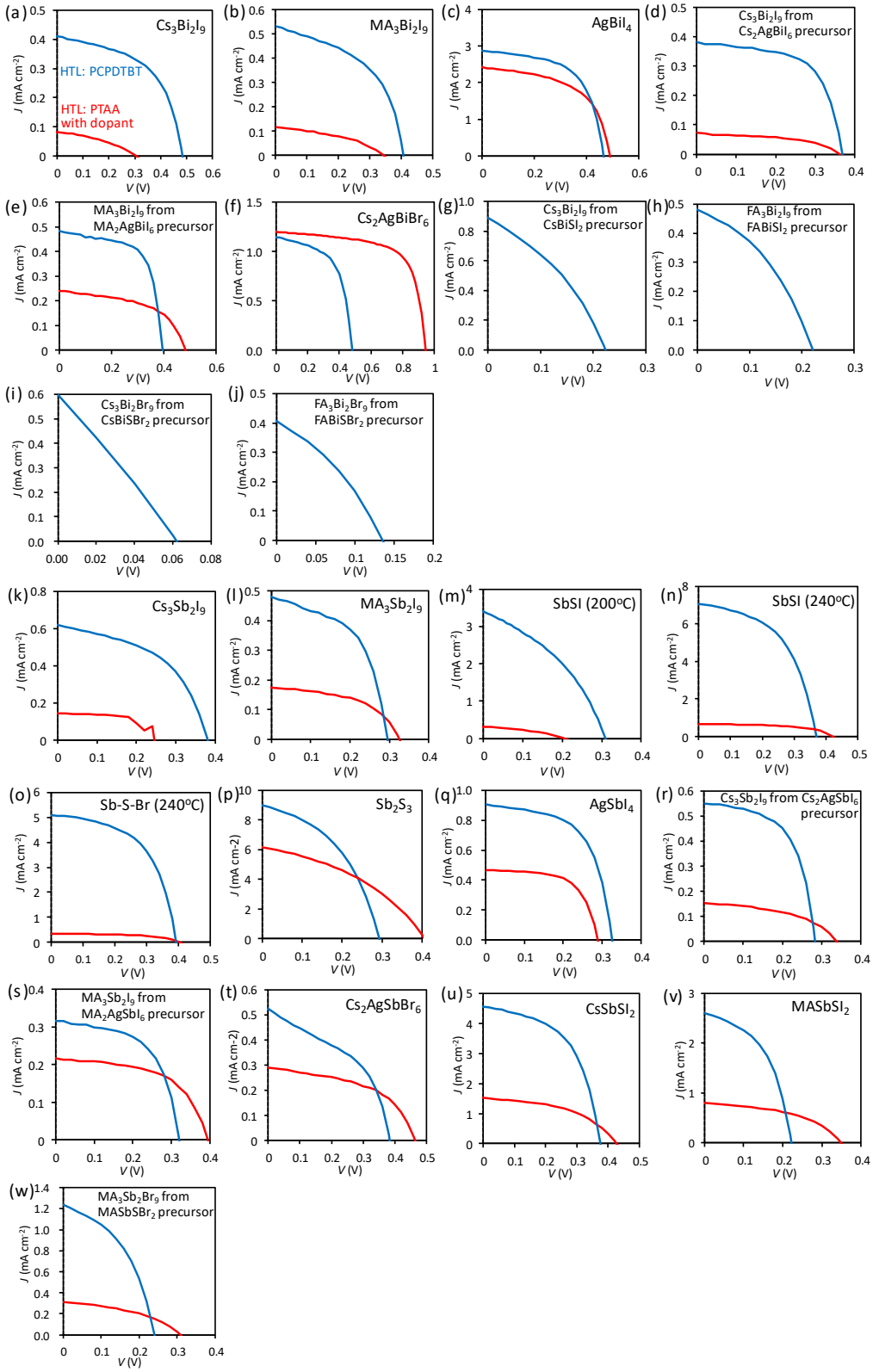

Figure S11. The *JV* curve of Bi and Sb-based solar cells which showed higher PCE than 0.01%. The colors of *JV* curve represent different HTMs, red line: PTAA with dopant, blue line: PCPDTBT. For $AgBiI_4$ and $AgSbI_4$, Li-TFSI and tBP was not included into PTAA to avoid dopant-induced degradation. The device structure is shown in Figure S15a.

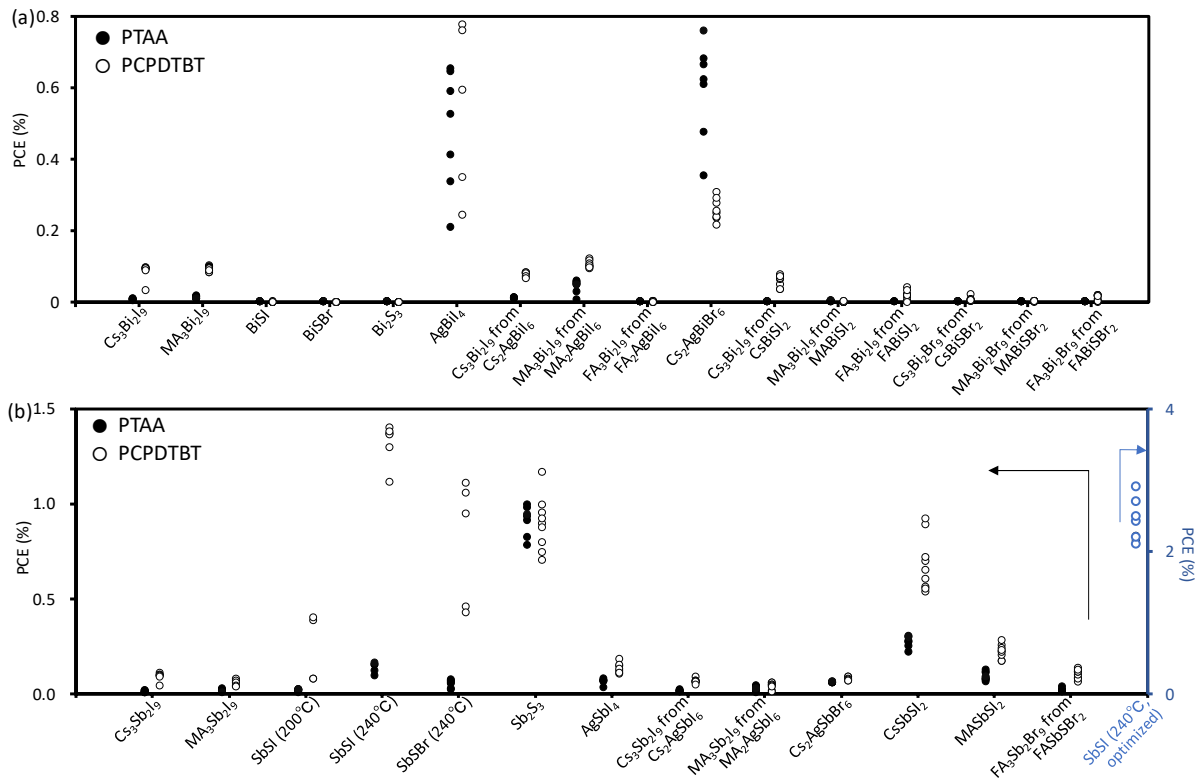

Figure S12. Statistics of solar cell performance of (a) Bi- and (b) Sb-based materials, which are corresponding to Table S5. The optimized Sb_2S_3-containing SbSI (at 240 °C), prepared by pre-deposition and double spin-coating, are described with blue circles in (b). For each device structure, 5~9 cells were measured.

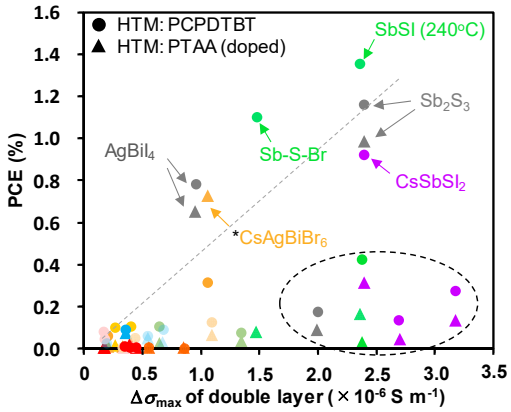

Figure S13. PCE vs $\Delta\sigma_{max}$ of double layer obtained from Xe-flash TRMC.

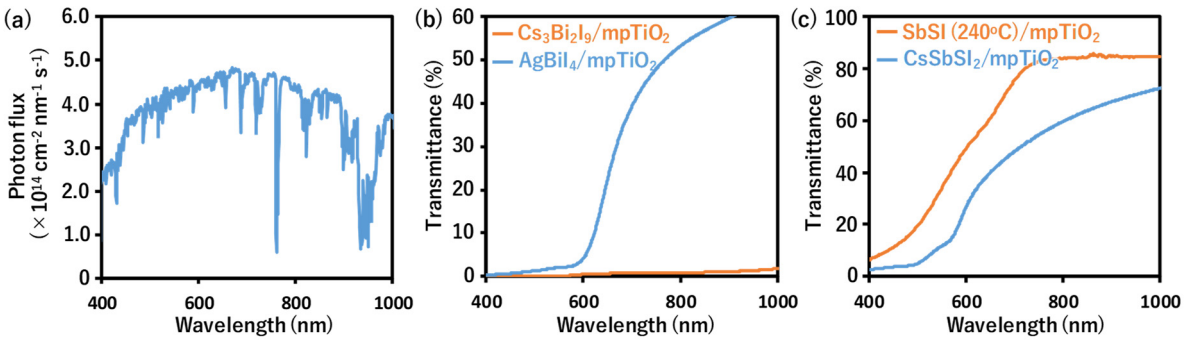

Figure S14. (a) Photon flux of AM1.5G sun light obtained from NREL[S8]. (b, c) Transmittance spectra of $Cs_3Bi_2I_9$, $AgBiI_4$, Sb_2S_3-containing SbSI (240 °C), and $CsSbSI_2$ on mp-TiO_2.

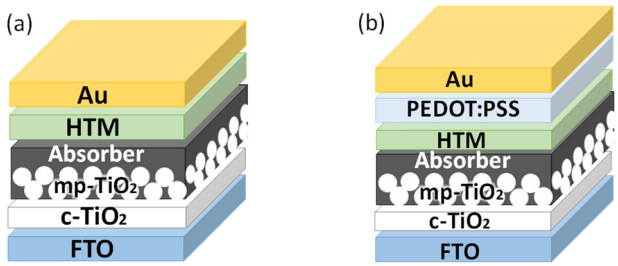

Figure S15. (a) Device structure used for the initial screening. (b) Optimized device structure of Sb_2S_3-containing SbSI device.

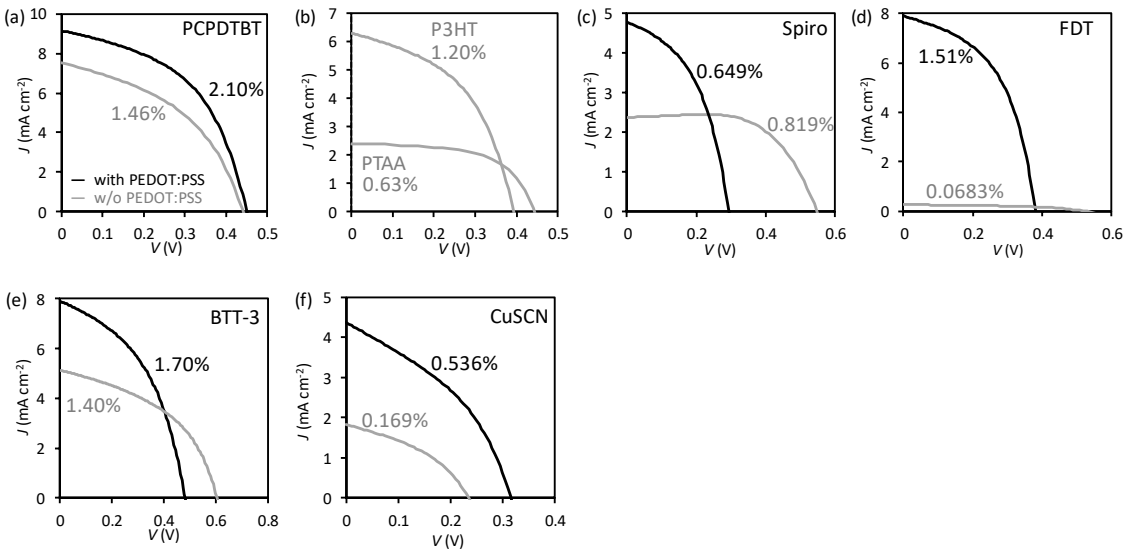

Figure S16. The *JV* curve of Sb_2S_3-containing SbSI based solar cells with different HTMs. The colors of *JV* curve represent inclusion of PEDOT:PSS layer between HTM and Au electrode, black line: with PEDOT:PSS (FTO/c-TiO_2/mp-TiO_2/SbSI/PCPDTBT/PEDOT:PSS/Au), gray line: without PEDOT:PSS (FTO/c-TiO_2/mp-TiO_2/SbSI/PCPDTBT/Au).

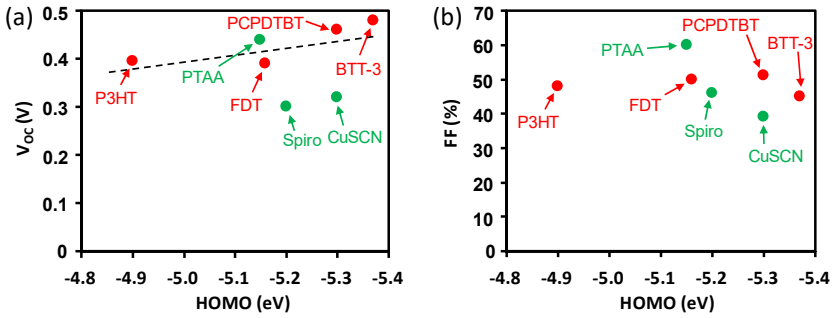

Figure S17. (a) V_{OC} and (b) FF vs. HOMO (or VBM) level of each HTM, which is corresponding to Figure 4.

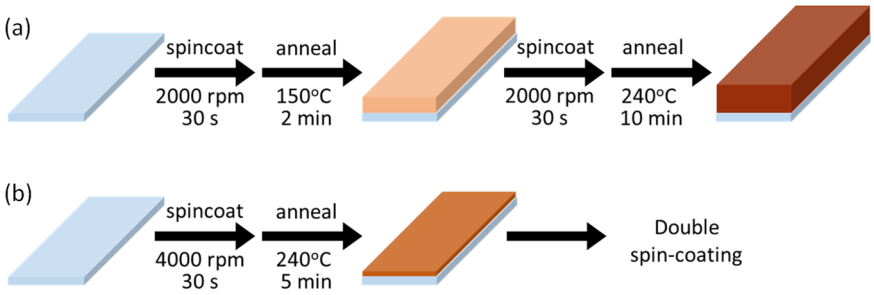

Figure S18. Schematic image of (a) double spin-coating and (b) pre-deposition of thin SbSI. The original precursor solution (SbI_3 0.4 M, $Sb(EtX)_3$ 0.3 M) was diluted with DMSO; (a) precursor : DMSO = 1 : 0.5, (b) precursor : DMSO = 1 : 3. The detail is as follows: (a) the diluted solution was spin-coated onto the substrate (2000 rpm, 30 s), followed by annealing (150 °C, 2 min). After cooling the substrate to room temperature, the precursor solution was spin-coated again (2000 rpm, 30 s), and annealed (240 °C, 10 min). (b) The diluted solution was spin-coated (4000 rpm, 30 s) followed by annealing (240 °C, 5 min). Then, SbSI was spin-coated again in the same manner with the process (a).

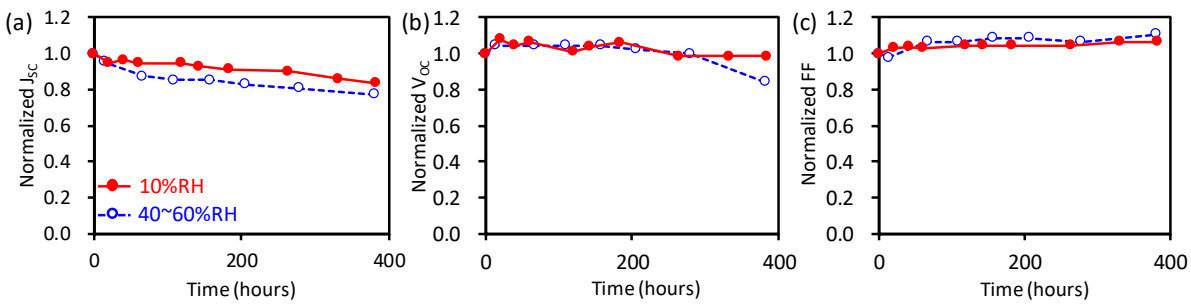

Figure S19. Normalized (a) J_{SC}, (b) V_{OC}, and (c) FF as a function of storage time in dried condition (~10%RH) and high humidity (40~60%RH) under room light.

Supporting Reference

(S1) Leng, M.; Chen, Z.; Yang, Y.; Li, Z.; Zeng, K.; Li, Z.; Niu, G.; He, Y.; Zhou, Q.; Tang, J. Lead-Free Blue Emitting Bismuth Halaide Perovskite Quantum Dots. *Angew. Chem. Int. Ed.* **2016**, *55*, 15012–15016.

(S2) Szklarz, P.; Jakubas, R.; Gagor, A.; Bator, G.; Cichos, J.; Kar-bowiak, M. $[NH_2CHNH_2]_3Sb_2I_9$: a lead-free and low-toxicity organic–inorganic hybrid ferroelectric based on antimony(III) as a potential semiconducting absorber. *Inorg. Chem. Front.* **2020**, *7*, 1780–1789.

(S3) Yang, J.-M.; Choi, E.-S.; Kim, S.-Y.; Kim, J.-H.; Park, J.-H.; Park, N.-G. Perovskite-related $(CH_3NH_3)_3Sb_2Br_9$ for forming-free memristor and low-energy-consuming neuromorphic computing. *Nanoscale* **2019**, *11*, 6453–6461.

(S4) Zhu, H.; Pan, M.; Johansson, M. B.; Johansson, E. M. J. High Photon-to-Current Conversion in Solar Cells Based on Light-Absorbing Silver Bismuth Iodide. *ChemSusChem* **2017**, *10*, 2592–2596.

(S5) Wei, F.; Deng, Z.; Sun, S.; Zhang, F.; Evans, D. M.; Kieslich, G.; Tominaka, S.; Carpenter, M. A.; Zhang, J.; Bristowe, P. D.; Cheetham, A. K. Synthesis and Properties of a Lead-Free Hybrid Double Perovskite: $(CH_3NH_3)_2AgBiBr_3$. *Chem. Mater.* **2017**, *29*, 1089−1094.

(S6) García-Espejo, G.; Rodríguez-Padrón, D.; Luque, R.; Camacho, L.; Miguel, G. Mechanochemical synthesis of three double perovskites: $Cs_2AgBiBr_6$, $(CH_3NH_3)_2TlBiBr_6$ and $Cs_2AgSbBr_6$. *Nanoscale* **2019**, *11*, 16650–16657.

(S7) Nie, R.; Mehta, A.; Park, B. W.; Kwon, H. W.; Im, J.; Seok, S. Il. Mixed Sulfur and Iodide-Based Lead-Free Perovskite Solar Cells. *J. Am. Chem. Soc.* **2018**, *140*, 872–875.

(S8) NREL Reference Air Mass 1.5 Spectra https://www.nrel.gov/grid/solar-resource/spectra-am1.5.html